Phase separation and magnetoresistivity in $Sm_{0.1}Ca_{0.9-x}Sr_xMnO_3$

C. Martin, A. Maignan, M. Hervieu, and S. Hébert
Laboratoire CRISMAT, UMR 6508 CNRS ENSICAEN, 6 bd Maréchal Juin, 14050 Caen Cedex, France

A. Kurbakov
Petersburg Nuclear Physics Institute, Orlova Grove, Gatchina, Leningrad District 188 300, Russia

G. André and F. Bourée-Vigneron
LLB, CEA-Saclay, 91191 Gif Sur Yvette, France

J. M. Broto, H. Rakoto, and B. Raquet
LNCMP, 143 Avenue de Rangueil, 31432 Toulouse Cedex, France
(Received 12 October 2007; published 1 February 2008)

The structural and physical properties of the electron-doped $Sm_{0.1}Ca_{0.9-x}Sr_xMnO_3$ perovskite manganites ($0 \leqslant x \leqslant 0.8$) have been studied by combining x-ray and neutron diffractions with measurements of magnetization (in static or pulsed magnetic fields), magnetic susceptibility, and resistivity. A structural change, from *Pnma* (for $x \leqslant 0.4$) to $I4/mcm$ ($0.5 \leqslant x < 0.8$), is observed at room temperature. A detailed study of two compounds ($x=0.3$ and 0.6), belonging to each structural region, demonstrates different phase separations at low temperature, with mixtures of *C*- and *G*-type antiferromagnetisms associated with different crystallographic structures ($P2_1/m$ for $x=0.3$ and $I4/mcm$ for $x=0.6$). The stabilization of different (crystallographic and magnetic) states together with the different Néel temperatures gives the opportunity to control the robustness of the antiferromagnetism versus *A*-site size parameters, such as $\langle r_A \rangle$ and σ^2. Since 50 T are not sufficient to collapse the antiferromagnetism in $Sm_{0.1}Ca_{0.3}Sr_{0.6}MnO_3$, a spontaneous magnetization is observed for $x < 0.2$. It is demonstrated that, also in Mn^{+4}-rich manganites, the magnetoresistive properties can be optimized by chemical pressure, the Sr for Ca substitution increasing the octahedra tilting in the *Pnma* structure.

DOI: 10.1103/PhysRevB.77.054402 PACS number(s): 75.25.+z, 71.30.+h, 61.05.F−

INTRODUCTION

The asymmetry of the magnetic and transport properties between hole- and electron-doped perovskite manganites partly results from their different concentrations of Jahn-Teller Mn^{3+} cations. The electric transport of the $Ln_{1-x}Ca_xMnO_3$ manganites is insulating in the paramagnetic (*P*) state on the hole-doped side ($x < 0.5$),[1,2] whereas on the electron-doped side, only a low concentration of Mn^{3+}, such as $x \geqslant 0.95$, is sufficient to induce metallicity.[3–6] In particular, the metallic behavior often reported for $CaMnO_3$ is understood by the existence of a slight oxygen nonstoichiometry responsible for the creation of electrons delocalized in an e_g narrow band.[7,8] Furthermore, the magnetism of electron-doped manganites differs also from that of hole-doped ones.[9,10] The ferromagnetism of the former exists only in a narrow range of Mn^{3+} concentration and corresponds to a magnetic phase separation between a G-type antiferromagnetic (AF) insulating matrix and ferromagnetic (F) metallic clusters.[11–15] The percolation of the latter enhances the metallicity below the Curie temperature. For all these manganites, the competition between the different ground states (metallic double-exchange ferromagnetism, superexchange antiferromagnetism, orbital order and disorder) is, however, not only controlled by the band filling but also by the effective one-electron bandwidth of the e_g band, that is, the Mn-O-Mn bond angles and Mn-O bond lengths, via the choice of the *A*-site cations (Ln, Ca). The key role of these structural parameters is exemplified by the comparison of two electron-doped manganites, $Sm_{0.1}Ca_{0.9}MnO_3$ and $Pr_{0.1}Sr_{0.9}MnO_3$, having the same Mn^{3+} concentration.[11] The former undergoes a magnetic transition from *P*- to *G*-type AF+F, without structural transition, whereas the latter exhibits magnetic and structural transitions from paramagnetic cubic to a mixture of two antiferromagnetic phases, *C*-type+*G*-type, crystallizing both in the $I4/mcm$ space group. The *C*-type AF is described as F files which are AF coupled, whereas in the *G*-type structure each Mn is AF coupled with its six Mn neighbors.[9,10] Thus, the *A*-site average ionic radius allows controlling the nature of the phase separation in the electron-doped manganites and, in principle, the amount of F phase. In order to study the change of electronic and magnetic ground states in the electron-doped manganites, the structural and magnetic properties of the $Sm_{0.1}Ca_{0.9-x}Sr_xMnO_3$ series have been investigated, by x-ray and neutron diffractions in connection with transport and magnetic measurements. The choice of the composition $Sm_{0.1}Ca_{0.9}MnO_3$ in the series $Sm_{1-x}Ca_xMnO_3$ is motivated by the larger amount of F component associated with the more metallic behavior for a manganese oxidation state of +3.9.

EXPERIMENTAL SECTION

The $Sm_{0.1}Ca_{0.9-x}Sr_xMnO_3$ samples have been prepared from $x=0$ to 0.2 by 0.02 step and from 0.2 to 1 by 0.1 step, by using a conventional synthesis process in air.[5,11] Stoichiometric ratios of Sm_2O_3, CaO, $SrCO_3$, and MnO_2 were weighted, mixed, and heated in air 12 h at 1000 °C. These powders were then crushed and pressed in the form of bars

and synthesized in two steps at 1200 and 1500 °C during 12 h with a slow cooling down to 800 °C. Two samples ($Sm_{0.1}Ca_{0.6}Sr_{0.3}MnO_3$ and $Sm_{0.1}Ca_{0.3}Sr_{0.6}MnO_3$) were also prepared in larger amounts (5 g) by using $^{152}Sm_2O_3$ as precursor, in order to perform neutron powder diffraction (NPD).

The purity of the samples was checked by x-ray powder diffraction (XRPD) at room temperature (RT) by using a Philips diffractometer (Cu $K\alpha$ radiations) and an angular range $10<2\theta<100°$ with 0.02° steps. The neutron powder diffraction study was performed in LLB-Saclay (France) for $Sm_{0.1}Ca_{0.6}Sr_{0.3}MnO_3$ and $Sm_{0.1}Ca_{0.3}Sr_{0.6}MnO_3$. The temperature dependence was followed from 1.4 to 300 K by using the G4.1 diffractometer ($\lambda=2.4245$ Å, from 14° to 94° in 2θ). A second set of measurements was performed with the 3T2 diffractometer ($\lambda=1.2261$ Å, from 4.15° to 121.95° in 2θ) at 300 K for both samples and at 500 K for $Sm_{0.1}Ca_{0.3}Sr_{0.6}MnO_3$. The G4.2 diffractometer ($\lambda=2.3426$ Å with $3°<2\theta<143°$) was also used for magnetic determinations at several temperatures (1.5, 60, 100, 135, and 150 K for $Sm_{0.1}Ca_{0.6}Sr_{0.3}MnO_3$ and 1.5, 90, and 150 K for $Sm_{0.1}Ca_{0.3}Sr_{0.6}MnO_3$). The diffraction data were refined with the FULLPROF suite.[16]

The magnetization curves $[M(T)]$ were recorded with a vibrating sample magnetometer ($T_{max}=300$ K) or a SQUID magnetometer ($T_{max}=400$ K), in increasing temperature and under 1.45 T [after a zero field cooling (zfc) or a field cooling (fc)]. The ac magnetic susceptibility data were recorded up to 350 K with an excitation field $h_{ac}=10$ Oe for frequencies $f=10^2$, 10^3, and 10^4 Hz, increasing or decreasing temperature.

Electrical resistances were measured, decreasing the temperature, with the four-probe technique, by using bars with typical dimensions $2\times2\times10$ mm^2, in a Physical Properties Measurements System (PPMS, Quantum Design), that also allows magnetic field scans in the range of 0–9 T.

Experimental measurements of transport and magnetization under high magnetic field were performed using the pulsed field facilities of the LNCMP (Toulouse, France). The magnetization experiments were performed using a classical compensated pickup coils technique. The signal was recorded during both the increasing and decreasing parts of the field at a constant temperature after a zfc procedure. Increasing time of the field is 25 ms and the total time of the field is 150 ms. The magnetoresistance is measured by the four-probe technique under ac current (3 kHz), in this case the increasing time of the field is 43 ms and total time 350 ms.

Thermopower was measured using a steady state technique in a home-made sample holder inserted in a PPMS.

RESULTS

Room temperature x-ray structural study

The refinements of the room temperature XRPD data show a transition from *Pnma* ($a_p\sqrt{2}\times2a_p\times a_p\sqrt{2}$) for $x\leq0.4$ to *I*4/*mcm* ($a_p\sqrt{2}\times a_p\sqrt{2}\times2a_p$) space group for $0.5\leq x<0.8$ (a_p referring to the cell parameter of cubic perovskite). For higher x values (≥0.8), a mixture of hexagonal and cubic phases is observed. In fact, it is well known that for such compounds (close to $SrMnO_3$), syntheses in reducing atmosphere are needed to avoid the hexagonal phases.[17–19] This part of the diagram being not of first importance for this study, no new samples have been prepared in the adequate conditions.

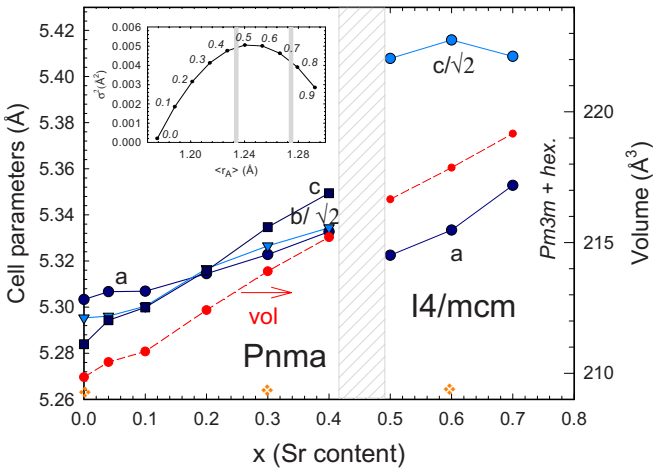

FIG. 1. (Color online) Cell parameters (left y axis) and volume (right y axis) versus the Sr content (x), Inset: Mismatch parameter (σ^2) versus the average A-site size $\langle r_A\rangle$) along the $Sm_{0.1}Ca_{0.9-x}Sr_xMnO_3$ series, the corresponding x values are given in the plot; r_A are taken from Ref. 20 in coordination IX and $\sigma^2=\Sigma x_i r_i^2-\langle r_A\rangle^2$. The crosses on the x axis indicate the compositions studied by neutron diffraction (this work and Ref. 11 for $x=0$).

The x dependence of the cell parameters and unit cell volume is shown Fig. 1. The volume increases regularly with x in agreement with the larger size of Sr^{+2} compared to Ca^{+2} (Ref. 20) but a clear discontinuity appears for the cell parameters, at the boundary between both structural domains (i.e., for $x\cong0.45$). The *Pnma* structures are slightly distorted (the distortion parameter $[(a+c)/b\sqrt{2}]$ remains close to 1), whereas the cell parameters present a clear splitting in the *I*4/*mcm* space group (leading to a distortion $[a\sqrt{2}/c]$ around 0.98). In the *Pnma* domain, the structure is pseudocubic, in agreement with the absence of cooperative Jahn-Teller effect due to the +3.9 valency of manganese;[21] nevertheless, two kinds of lattices are observed, $a>b/\sqrt{2}>c$ for $x<0.2$ and $c>b/\sqrt{2}>a$ for $x>0.2$. This evolution is due to a smaller and a larger increase of a and c, respectively, when the Sr content increases. The slight x dependence of a is in agreement with a low and constant amount of Jahn-Teller Mn^{3+} and the increase of c reflects an increase of the octahedral tilting.[22]

In this $Sm_{0.1}Ca_{0.9-x}Sr_xMnO_3$ series, the average A-site cation size ($\langle r_A\rangle$) increases regularly with x, but the mismatch values (σ^2, reflecting the disorder induced by several cations with different sizes on the same crystallographic site[23,24]) go through a maximum for $x=0.5$ (Fig. 1, inset), which can be thus associated with the *Pnma* to *I*4/*mcm* structural transition. Such an evolution from *Pnma* to *I*4/*mcm*, at fixed Mn valency, was previously observed in various series. It differs from the results obtained for $Pr_{0.5}Sr_{0.5-x}Ca_xMnO_3$ where an *Imma* domain is observed (for a small x range) between the *Pnma* and *I*4/*mcm* areas,[25] but it is similar to the one re-

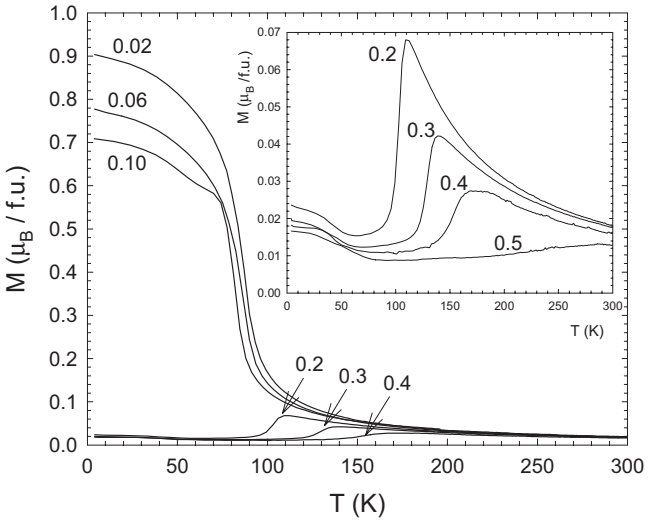

FIG. 2. Temperature dependence of the magnetization $[M(T)]$ for samples of the series $Sm_{0.1}Ca_{0.9-x}Sr_xMnO_3$ (zfc, 1.45 T), x values are given in the figure; Inset: Enlargement showing the development of a broad small maximum at high temperature.

ported for the $Ca_{1-x}Sr_xMnO_3$ system.[19] Nevertheless, the *Pnma* to $I4/mcm$ transition appears at lower $\langle r_A \rangle$ in the title series, in connection with its larger σ^2 values due to the small size of Sm^{+3} compared to Ca^{+2} and Sr^{+2}.

Magnetic properties

Magnetization and susceptibility

The magnetization data as a function of temperature (Fig. 2) recorded up to 300 K (zfc process, 1.45 T) show that the F component, corresponding to about $\sim 1\mu_B$/f.u. for $Sm_{0.1}Ca_{0.9}MnO_3$, is very sensitive to the strontium for calcium substitution, and seems to be totally suppressed as soon as 0.2 Sr are substituted for Ca (i.e., $x=0.2$ in the figure). This "upper" x limit for the F component corresponds to the crossing point $a \cong c \cong b/\sqrt{2}$ observed in Fig. 1. As described in the Introduction, the magnetic ground state of $Sm_{0.1}Ca_{0.9}MnO_3$ at low temperature corresponds to F clusters embedded in a G-type AF matrix. Its magnetic signature in the macroscopic measurements is the existence of a sharp peak on the magnetic susceptibility curves collected with a low ac magnetic field (10 Oe), developing just below $T_N = T_C = 110$ K, followed by a broad χ shoulder as T decreases.[4] In this lower temperature range, the ac-χ' depends on the frequency (f) of the excitation of the magnetic field, as shown for $Sm_{0.1}Ca_{0.8}Sr_{0.1}MnO_3$ (Fig. 3, inset). The $\chi'(T)$ curves of the $Sm_{0.1}Ca_{0.9-x}Sr_xMnO_3$ samples (Fig. 3), where χ' values are given in a logarithmic scale, show that the cluster-glass (CG) characteristic shape of the $\chi'(T)$ curve is still present for up to $Sm_{0.1}Ca_{0.72}Sr_{0.18}MnO_3$, with T_C values kept roughly unchanged, though the χ' magnitude has dropped by 1 order of magnitude. For this small x range ($x = 0.10$ and 0.18 in Fig. 3), the $\chi'(T)$ curves exhibit a strong increase at low temperature ($T < 15$ and 10 K, respectively) whose origin remains unclear. However, as shown from the

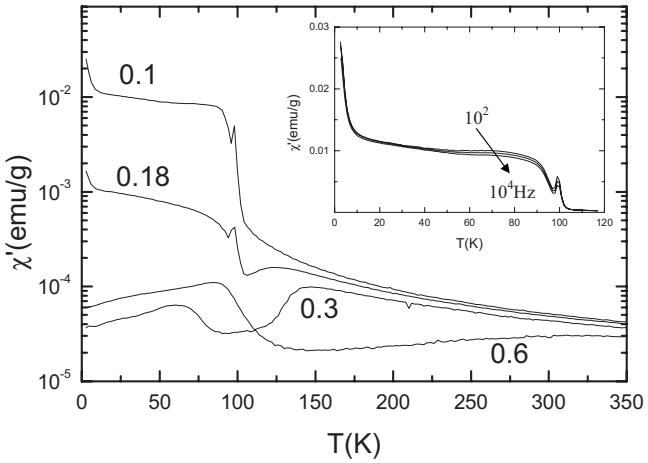

FIG. 3. $\chi'(T)$ curves of selected samples of the series $Sm_{0.1}Ca_{0.9-x}Sr_xMnO_3$ (x values are labeled in the graph) 10 Oe; 10^4 Hz and decreasing temperature. Inset: T dependence of the ac magnetic susceptibility (real part, χ') of $Sm_{0.1}Ca_{0.8}Sr_{0.1}MnO_3$ ($x=0.1$), 10 Oe and $10^2, 10^3, 10^4$ Hz and increasing temperatures.

$M(T)$ curves (Fig. 2, inset), the Sr for Ca substitution generates an additional magnetization broad maximum developing at higher temperature. This feature is also well defined at 120 K on the $\chi'(T)$ curve for $Sm_{0.1}Ca_{0.72}Sr_{0.18}MnO_3$ (Fig. 3). The characteristic temperature of this maximum shifts up progressively with x, reaching 315 K for $x=0.6$ (Fig. 4). Both characteristic temperatures increase thus with the Sr content; the low transition temperature evolves from 70 K ($x=0.3$) to 120 K ($x=0.6$) and the higher one moves from 140 K ($x=0.3$) to 315 K ($x=0.6$). The lower temperature transition is associated with a field cooled and/or zero field cooled effect which is clearly shown in inset by the susceptibility curves measured in 100 Oe (Fig. 4, inset). This behavior is characteristic of ferromagnetic interactions at

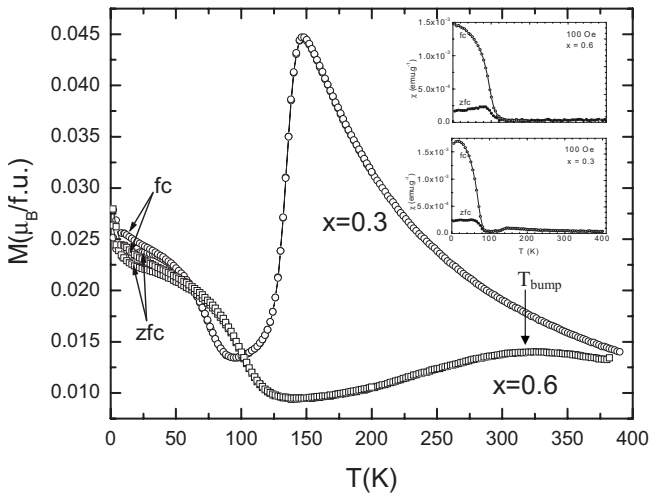

FIG. 4. $M(T)$ curves collected up to 375 K for $Sm_{0.1}Ca_{0.6}Sr_{0.3}MnO_3$ ($x=0.3$) and $Sm_{0.1}Ca_{0.3}Sr_{0.6}MnO_3$ ($x=0.6$) (1.45 T, fc and zfc modes). In inset the temperature dependences of susceptibility (deduced from magnetization measurements) for both samples are given in 100 Oe, field and zero field cooling.

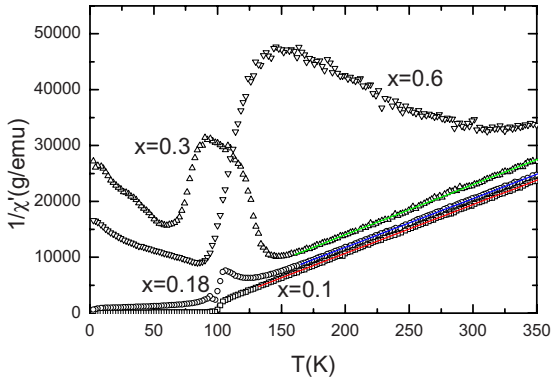

FIG. 5. (Color online) Inverse magnetic susceptibility $[\chi'^{-1}(T)]$ curves of four samples of the $Sm_{0.1}Ca_{0.9-x}Sr_xMnO_3$ series. The solid lines are the fitted curves of the linear parts.

low temperature even for the $x=0.6$ composition. The rapid decrease of this F component with the Sr increase goes with the decrease of θ_p determined from the linear part of the inverse susceptibility curves $\chi'(T)$ (Fig. 5), from 78 K for $Sm_{0.1}Ca_{0.8}Sr_{0.1}MnO_3$ down to 44 K for $Sm_{0.1}Ca_{0.6}Sr_{0.3}MnO_3$. For larger Sr content, the lack of linear regime (up to 350 K) precludes the extrapolation of the $\chi'(T)$ curve as shown for the $x=0.6$ composition in Fig. 5. All the determined θ_p values are positive, characterizing thus ferromagnetic interactions. Nevertheless, the AF state stabilized at low temperature is robust, as shown by the $M(H)$ curves collected at 5 K up to 5 T in Fig. 6 (insets) for $x=0.3$ and 0.6. The fact that the maximal magnetization values remain small in 5 T has motivated magnetization measurements under high magnetic fields for both compounds ($x=0.3$ and 0.6) studied by neutron diffraction.

The magnetization curves recorded under magnetic field up to 50 T from 4.2 K to room temperature are reported in Fig. 6. In the case of $x=0.6$, the magnetization is essentially linear up to 50 T for all temperatures, characteristic of an AF state, with magnetization values far below the saturation value for Mn. The compound with $x=0.3$ presents below T_N ($\cong$140 K) metamagnetic transitions with a hysteresis between the sweep-up and sweep-down measurements, wider when the temperature is lower. The characteristic magnetic field of the AF to F transition decreases from 45 T at 4.2 K down to 27 T at 110 K. The saturation of the magnetization corresponding to the F state is never reached whatever the temperature at the maximum magnetic field. At low field and low temperature, only a small deviation of the linear variation is observed, which could be due to a small canting. These measurements clearly evidence that the Sr for Ca substitution stabilizes the AF state. For $Sm_{0.1}Ca_{0.3}Sr_{0.6}MnO_3$, this state cannot be destroyed by a magnetic field as high as 50 T; in the case of $Sm_{0.1}Ca_{0.6}Sr_{0.3}MnO_3$, the application of a high magnetic field can induce a transition toward a ferromagnetic state.

Neutron diffraction study

The neutron diffraction study first confirms the space groups evidenced by x-ray diffraction at RT for

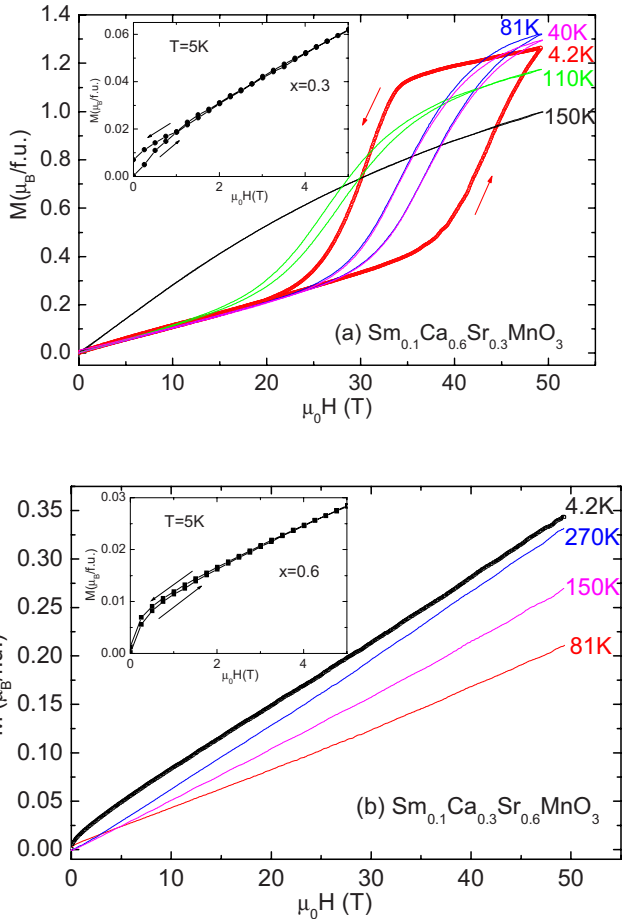

FIG. 6. (Color online) High field magnetization curves at several temperatures for $Sm_{0.1}Ca_{0.6}Sr_{0.3}MnO_3$ (a) and $Sm_{0.1}Ca_{0.3}Sr_{0.6}MnO_3$ (b). Magnetic field dependence $M(H)$ curves collected at 5 K and up to 5 T are also given in inset.

$Sm_{0.1}Ca_{0.6}Sr_{0.3}MnO_3$ (*Pnma*) and $Sm_{0.1}Ca_{0.3}Sr_{0.6}MnO_3$ (*I*4/*mcm*). The temperature dependence of the NPD patterns is reported in Figs. 7(a) and 7(b), respectively. It shows two magnetic transitions without structural ones for $Sm_{0.1}Ca_{0.3}Sr_{0.6}MnO_3$. At $\approx$240 K, peak characteristics of *C*-type AF start to develop and at $\approx$120 K, a peak characteristic of *G*-type AF appears [Fig. 7(b)]. The magnetic behavior of $Sm_{0.1}Ca_{0.6}Sr_{0.3}MnO_3$ is similar, with *C*- and *G*-type AFs establishing at $\approx$150 and 70 K, respectively. Nevertheless, for this compound a structural transition is associated with the magnetic one at 150 K (from *P*-*Pnma* to *C*-AF-$P2_1/m$) [Fig. 7(a)]. In both cases, no clear F component is evidenced whatever the temperature. The T_N(G)'s determined by neutron diffraction correspond to the lower characteristic temperatures observed in the magnetization curves for both compounds (Fig. 4). In contrast, if the T_N(C) of $Sm_{0.1}Ca_{0.6}Sr_{0.3}MnO_3$ fits well with the kink evidenced in the $M(T)$ curve, there is no clear correspondence between T_N(C) of $Sm_{0.1}Ca_{0.3}Sr_{0.6}MnO_3$ ($\cong$240 K) and the bump observed in the $M(T)$ curve at higher temperature. This point will be discussed later. The temperature dependences of the crystalline and magnetic structures were analyzed by using the medium resolution G4.1 data rows and consequently with only

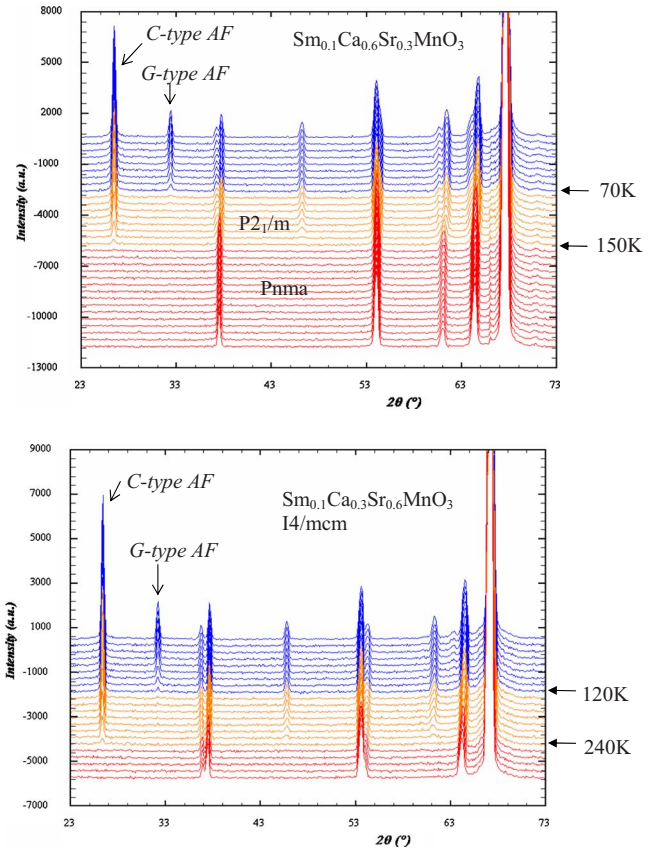

FIG. 7. (Color online) Temperature dependence (from 1.4 to 300 K) of NPD patterns [G4.1, $\lambda=2.4245$ Å] observed for (a) $Sm_{0.1}Ca_{0.6}Sr_{0.3}MnO_3$ and (b) $Sm_{0.1}Ca_{0.3}Sr_{0.6}MnO_3$. This enlargement, from 23° to 73° in 2θ, was chosen to highlight the magnetic peaks.

one crystallographic phase for each temperature. Nevertheless, these calculations, completed by the 3T2 and G4.2 data, lead to a coherent picture.

The room temperature crystallographic parameters were first obtained from analysis of the high resolution 3T2-NPD data, whose results agree with the preliminary x-ray study. The quality of the fit is attested in Figs. 8(a) and 8(b) for the $x=0.3$ and 0.6 compositions, respectively, and the corresponding crystallographic parameters are summarized in Table I. For both compounds, the actual compositions seem to be very close to the nominal ones. Due to the occupancy of the A site of the perovskite by three cations with coherent scattering length of -0.50, 0.49, and 0.702 ($\times 10^{-12}$ cm) for ^{152}Sm, Ca, and Sr respectively, and to the absorption cross section of ^{152}Sm, successive trials were performed to check the occupancy of this site and they did not show any evidence of deviation from the expected formula. A careful attention was also paid to the oxygen content, and the calculations lead to oxygen stoichiometric samples.

The structure of $Sm_{0.1}Ca_{0.6}Sr_{0.3}MnO_3$—refined in the *Pnma* space group—is very regular, leading to slightly compressed MnO_6 octahedra: the apical interatomic Mn-O distances (1.903 Å) are slightly smaller than the equatorial ones (1.906 and 1.909 Å). These results obtained at room temperature are similar to those reported for $Sm_{0.1}Ca_{0.9}MnO_3$.[11] The space group is the same and the cell parameters are close but the increase of the cell volume due to the larger size of strontium, compared to calcium, is not reflected in the MnO_6 size. In fact, the shape of the octahedra is similar (slightly compressed) but the Mn-O distances are smaller in $Sm_{0.1}Ca_{0.6}Sr_{0.3}MnO_3$ in connection with an increase (of around 5°) of the Mn-O1-Mn angles. This evolution is clearly different from the one observed between $Sm_{0.1}Ca_{0.9}MnO_3$ and $Sm_{0.15}Ca_{0.85}MnO_3$ (Ref. 26) for which the lattice volume increase (due to the increase of the Mn^{3+} amount) maintains the MnO_6 distortion with a slight increase of all the Mn-O distances without variation in the Mn-O1-Mn angles. It clearly shows the strong impact of $\langle r_A \rangle$ and σ^2 upon the structure.

For $Sm_{0.1}Ca_{0.3}Sr_{0.6}MnO_3$, due to a small anisotropic broadening of Bragg peaks, using in the refinements of microstrain parameters[16,27] allows an improvement of the fit in $I4/mcm$. Nevertheless, the higher strain parameter, that is, S_220, remains small [0.42(6), with a Lorentzian strain coefficient of 0.34(1)]. Moreover, the value obtained for the O1 thermal factor remains slightly high (0.94 Å^2), and is probably associated with an oxygen disorder. Refinements of anisotropic thermal parameters of oxygen improve slightly the fit [$R_p=1.94$, $R_{wp}=2.49$, and $R_{exp}=1.59\%$] without any noticeable changes in the crystallographic parameters and the B_{equi}. A small value of mean square displacement is observed along the z axis (0.05 Å), whereas larger values (0.13 Å) are refined along the (x,y) diagonal. These results are in good agreement with the observations reported for high mismatched manganites[24] but our last refinements should be taken with caution due to the numerous refined parameters. The distortion of the MnO_6 octahedra is different from the one observed for $x=0.3$, since they are elongated along the c axis (with apical Mn-O distances of 1.913 Å for four distances of 1.897 Å in the basal plane).

The structural and magnetic transitions are then followed by using the G4.1 patterns (Fig. 7). Dealing with the $x=0.3$ sample, at about 150 K, C-type AF appears, associated with a *Pnma* to $P2_1/m$ structural transition, going with a small increase of the a and c parameters and a stronger decrease of the b one. At lower temperature, that is, around 70 K, the G-type AF starts to develop, without visible structural changes. The low temperature state (<70 K) is thus described with one monoclinic cell associated with two antiferromagnetic components (with about $2\mu_B$ and $1\mu_B$ for C and G, respectively). The high resolution—G4.2—NPD data allow an improvement of the fit by adding a second crystalline phase of *Pnma* space group, corresponding to the G-type AF. At 1.5 K, the main part of the sample (≈95%) corresponds to the $P2_1/m$ space group and is associated with the C-type AF. The small amount of *Pnma*, the overlap of the Bragg peaks belonging to both phases (*Pnma* and $P2_1/m$) due to the closeness of their cell parameters ($a_p\sqrt{2}\times 2a_p\times a_p\sqrt{2}$), and the fact that F appear in addition to the nuclear peaks make unrealistic the complete refinement of both structures with our data; it is why only the parameters corresponding to the main $P2_1/m$ phase are reported in Table II. The magnetic moments ($2.1\mu_B$) are lying in the basal (x,z) plane in agreement with the distortion of the cell in this plane. The two

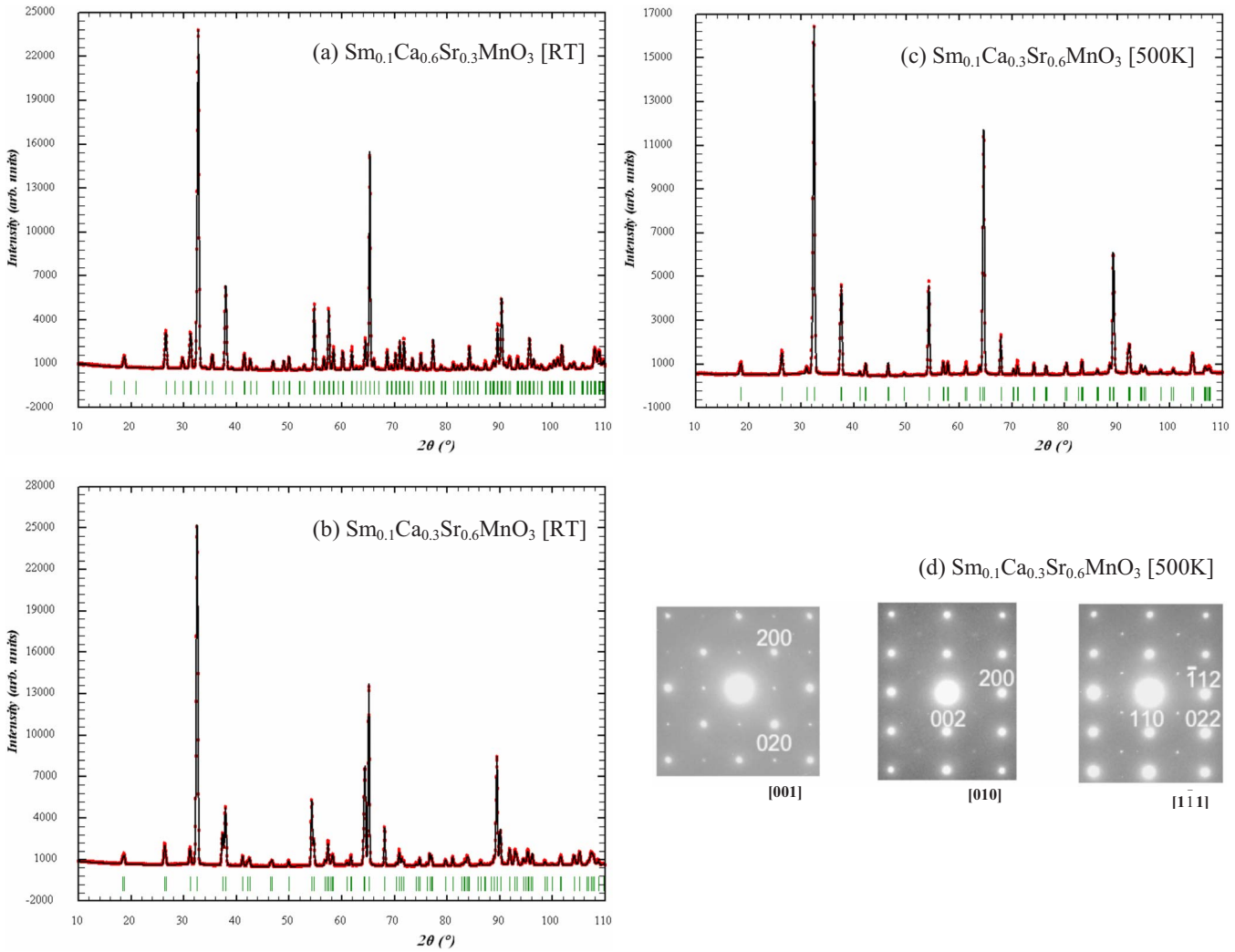

FIG. 8. (Color online) 3T2 (λ=1.2261 Å) neutron diffraction patterns (calculated, dark solid line; experimental, red points and Bragg ticks) of $Sm_{0.1}Ca_{0.6}Sr_{0.3}MnO_3$ (a) and $Sm_{0.1}Ca_{0.3}Sr_{0.6}MnO_3$ (b) measured at room temperature; of $Sm_{0.1}Ca_{0.3}Sr_{0.6}MnO_3$ at 500 K (c) and corresponding [001], [010], and [$1\bar{1}1$] ED patterns, characteristic of $I4/mcm$.

MnO_6 octahedra of this monoclinic phase exhibit the same distortion: the smaller distance is the apical Mn-O (1.890 Å in both cases) and one of the equatorial ones is longer (1.920 or 1.921 Å) than the other one (1.896 or 1.895 Å). This elongation is associated with the $d_{3z^2-r^2}$ orbital polarization, characteristic of *C*-type AF. Thus decreasing the temperature, the MnO_6 octahedra become more flattened and a strong distortion appears in the basal plane.

These results are different from those observed for $Sm_{0.1}Ca_{0.9}MnO_3$ (Ref. 11) that remains *Pnma* and does not exhibit *C*-AF, but are reminiscent of those reported for $Sm_{0.15}Ca_{0.85}MnO_3$ (Ref. 26) with a mixture of $P2_1/m$-*C* and *Pnma*-*G* AF at low temperature. The main difference deals with the characteristic temperatures T_N (*C* and *G*) very close in the case of $Sm_{0.15}Ca_{0.85}MnO_3$ (about 110 K) but differing by about 80 K in $Sm_{0.1}Ca_{0.6}Sr_{0.3}MnO_3$ (150 and 70 K for *C* and *G*, respectively). The competition between both magnetic orders is thus clearly different, due to the strong stabilization of the *C*-type AF in $Sm_{0.1}Ca_{0.6}Sr_{0.3}MnO_3$. It is difficult to exclude the existence of F in $Sm_{0.1}Ca_{0.6}Sr_{0.3}MnO_3$, due to the fact that such component induces only an increase of intensity on nuclear peaks and because the amount of *Pnma* phase (better adapted for F than $P2_1/m$) is small. These observations fit pretty well with the results of magnetization under high magnetic field, and also with those previously reported for the $Sm_{1-x}Ca_xMnO_3$ series.[28] In fact, the 4.2 K-$M(H)$ curve of $Sm_{0.1}Ca_{0.6}Sr_{0.3}MnO_3$ is clearly different from the one of $Sm_{0.1}Ca_{0.9}MnO_3$ (despite the same Mn valency) but mimics the one of $Sm_{0.15}Ca_{0.85}MnO_3$. For the latter, a small F component is first observed at low fields, which does not exist for $Sm_{0.1}Ca_{0.6}Sr_{0.3}MnO_3$, showing the disappearance of F interactions induced by the Sr for Ca substitution. At higher fields, a metamagnetic transition occurs in both compounds, but the critical field is higher for $Sm_{0.1}Ca_{0.6}Sr_{0.3}MnO_3$ (about 45 T) than $Sm_{0.15}Ca_{0.85}MnO_3$ (about 13 T in sweep-up process).

The data recorded with G4.1 for $Sm_{0.1}Ca_{0.3}Sr_{0.6}MnO_3$ were all refined by using one phase with the $I4/mcm$ space group and *C*-type and then *G*-type antiferromagnetic structures were added for $T \leqslant 240$ and 120 K, respectively [lead-

TABLE I. Room temperature crystallographic parameters (from 3T2 data). In *Pnma* (SG 62), the positions are Mn in $4b-(0,0,1/2)$; (Sm,Ca,Sr) in $4c-(x,1/4,z)$; O1 in $4c-(x,1/4,z)$; O2 in $8d-(x,y,z)$. In *I*4/*mcm* (SG 140), the positions are Mn in $4c-(0,0,0)$; (Sm,Ca,Sr) in $4b-(1/2,0,1/4)$; O1 in $4a-(0,0,1/4)$; O2 in $8h-(x,1/2+x,0)$.

Space group	$Sm_{0.1}Ca_{0.6}Sr_{0.3}MnO_3$ *Pnma*	$Sm_{0.1}Ca_{0.3}Sr_{0.6}MnO_3$ *I*4/*mcm*
a (Å)	5.32425 (7)	5.33548 (3)
b (Å)	7.53383 (7)	
c (Å)	5.33510 (9)	7.65127 (5)
V (Å^3)	214.002(5)	217.812(2)
Mn		
B (Å^2)	0.06(2)	0.03(2)
(Sm,Ca,Sr)		
x	0.0173(4)	
z	−0.0025(7)	
B (Å^2)	0.47(2)	0.37(1)
O1		
x	0.4947(4)	
z	0.0502(4)	
B (Å^2)	0.56(2)	0.94(2)
O2		
x	0.2784(2)	0.27705(8)
y	0.274(2)	
z	−0.2779(2)	
B (Å^2)	0.69(2)	0.71(1)
R_p, R_{wp}, R_{exp} (%)	2.93, 3.76, 1.53	2.83, 3.74, 1.60
Mn-O1 (Å)	1.9030 (3) (×2)	1.913 (×2)
Mn-O2 (Å)	1.909 (12) (×2)	1.8980 (4) (×4)
Mn-O2 (Å)	1.906 (12) (×2)	
Mn-O1-Mn (°)	163.72 (7)	180.00
Mn-O2-Mn (°)	162.14 (8)	167.44 (3)

ing to manganese magnetic moments of ≅2 and 1.1μ_B, respectively, (at 1.4 K)]. The temperature dependence of the lattice parameters was studied from 1.4 to 300 K (not shown) showing a smooth evolution, comparable with those of $Pr_{0.1}Sr_{0.9}MnO_3$; *a* increases and *c* slowly decreases as the temperature increases, but $Pr_{0.1}Sr_{0.9}MnO_3$ is cubic at RT (Ref. 11) that is not the case for $Sm_{0.1}Ca_{0.3}Sr_{0.6}MnO_3$. The low temperature structure was then analyzed by using the higher resolution NPD-G42 data. Two *I*4/*mcm* unit cells, whose parameters are reported in Table II, are used to describe the low temperature state. Both unit cells are elongated along the *c* axis, the more distorted one corresponds to the main phase (70%) and *C*-type AF (with 2.3μ_B) and the more regular one (30%) is associated with *G*-type AF (2.4μ_B). The magnetic moments are along the *c* axis, corresponding to the longer Mn-O distances in the *C*-AF phase, and perpendicular to this axis in the *G*-type phase.

These observations are similar to what was reported for $Pr_{0.1}Sr_{0.9}MnO_3$,[11] with mixtures of *C*- and *G*-AFs in *I*4/*mcm* phases with close distortions. In both cases, the *C*-type Néel temperatures (300 K for $Pr_{0.1}Sr_{0.9}MnO_3$ and 240 K for $Sm_{0.1}Ca_{0.3}Sr_{0.6}MnO_3$) are higher than the $T_N(G)$ (220 and 120 K, respectively). All characteristic temperatures are thus lower for $Sm_{0.1}Ca_{0.3}Sr_{0.6}MnO_3$ but the difference $[T_N(C)-T_N(G)]$ is larger, showing the structural effect due to the Sr for Ca substitution upon the stability of the magnetic phases in competition, particularly the destabilization of the *G*-type. Despite this effect on the Néel temperatures, the description of a microscopic phase separation in two elastically coupled phases proposed for the Pr compound seems available for the manganite under study. Nevertheless, to complete the structural study and in order to understand the broad kink in the $M(T)$ curve at temperatures higher than 300 K, a high resolution 3T2-NPD measurement was performed at 500 K. It shows that the tetragonal distortion of the structure decreases, though at 500 K the transition is not complete [Fig. 8(c)]. The best fit is obtained by refining the NPD diagram in *I*4/*mcm*, but with a small tetragonal distortion, very close to one, corresponding to the refined cell parameters

TABLE II. Low temperature (1.5 K) crystallographic parameters (from G4.2 data).

Space group	$Sm_{0.1}Ca_{0.6}Sr_{0.3}MnO_3$ (≅95%) $P2_1/m$	$Sm_{0.1}Ca_{0.3}Sr_{0.6}MnO_3$ (70%) *I*4/*mcm*	$Sm_{0.1}Ca_{0.3}Sr_{0.6}MnO_3$ (30%) *I*4/*mcm*
a (Å)	5.3224 (1)	5.304 46 (5)	5.304 46 (5)
b (Å)	7.4801 (2)		
c (Å)	5.3353 (1)	7.685 7 (4)	7.669 1 (7)
β (°)	90.767 (2)		
V (Å^3)	212.391 (9)	216.25 (1)	215.79 (2)
M (μ_B)	C_{xz} 2.08 (2)	C_z 2.34 (8)	G_{xy} 2.4(2)
Mn1-O1 (Å)	1.890 (1) ×2	1.921 ×2	1.917 ×2
Mn1-O2 (Å)	1.896 (2) ×2	1.890 (1) ×4	1.890 (1) ×4
Mn1-O2 (Å)	1.920 (2) ×2		
Mn2-O1 (Å)	1.890 (1) ×2		
Mn2-O2 (Å)	1.895 (2) ×2		
Mn2-O2 (Å)	1.921 (2) ×2		

$a=5.372\,36(4)$ and $c=7.621\,83(8)$ Å. No more anisotropic broadening of the peaks is observed, in agreement with the more cubic metric of the lattice; the fact that the B factors are high (1.47 and 1.28 $Å^2$ for O1 and O2, respectively) is difficult to discuss due to the temperature (500 K). To finish the structural characterization of this $x=0.6$ sample, it was then studied by transmission electron microscopy, from 300 to 500 K. The bright field images show the very good crystallinity of the sample. The electron diffraction confirms the $I4/mcm$-type structure at room temperature as well as the existence of twinning domains resulting from the tetragonal distortion of the perovskite cell. By increasing slightly the temperature, the reflections keep a pointlike shape and remain characteristics $I4/mcm$ up to 500 K as shown in Fig. 8(d).

The origin of the bump above RT in the magnetization curves is thus not due to the structural transition nor long range magnetic ordering. As explained in the case of the Bi-based manganites,[29] it could be accounted for by the switch from F to AF fluctuations.

Transport properties

The interplay between charge and spins is illustrated in Fig. 9(a) by selected T-dependent resistivity $\rho(T)$ curves. The metallic state associated with the CG for $Sm_{0.1}Ca_{0.9}MnO_3$ is already suppressed for $Sm_{0.1}Ca_{0.8}Sr_{0.1}MnO_3$ [$x=0.1$ in Fig. 9(a)] for which the resistivity shows an increase as the temperature decreases. This tendency toward localization at low temperature becomes more pronounced with the Sr content increase, as shown in the $x=0.2$ curve by the strong increase of ρ below $\cong 120$ K. This temperature is in good coincidence with the T_N of the C-type AF state, taken at the top of the peak in the magnetization curve (Fig. 2). Finally, the resistivity increases continuously with the decrease of temperature from 400 K for $x=0.6$ [Fig. 9(a), inset], consistently with the $M(T)$ curve (Fig. 5). For this compound, the magnetic transition corresponding to the C-type order is better seen in the derivative curve whereas the T_{bump} and the G-type magnetic one are clearly visible in the resistivity curve. As expected, the rapid disappearance of the metallic F clusters has a strong impact on the resistivity. Nonetheless, it must be pointed out that in the paramagnetic state the resistivity keeps similar values $\cong 2$ mΩ cm whatever the Sr content is, showing that if the magnetic exchange energies are sensitive to $\langle r_A \rangle$, this is not the case for the mechanism of electron delocalization in the disordered magnetic state.

According to previous reports on the negative magnetoresistance of electron-doped manganites, the coexistence of the G- with C-type AFs in the vicinity of existence of F component is necessary to reach the best effects. Since the Sr for Ca substitution allows to control (F/G-AF)/(C-AF) amounts, the MR vs x goes through a maximum, as shown by the $[\rho_0/\rho_{7\ \mathrm{T}}](T)$ curves [Fig. 9(b)] showing the highest value for $x=0.16$. In contrast, for the heavily Sr substituted samples ($x=0.6$), the MR has almost totally disappeared.

The $R(H)$ curves measured up to 50 T for $Sm_{0.1}Ca_{0.6}Sr_{0.3}MnO_3$ show a transition for $T<150$ K (Fig. 10). Even if the decrease of the resistivity reaches almost 2 orders of magnitude at 4.2 K, no metallic state is induced by the magnetic field application. In fact, the percolation threshold is probably not attained, in agreement with the magnetic field induced ferromagnetic component ($1.2\mu_B$/f.u.) that remains far from the theoretical one ($3.1\mu_B$/f.u.) even in 50 T (Fig. 6). The characteristic magnetic fields, deduced from magnetization and resistivity curves, are in good agreement. The transitions observed for $T<150$ K are thus attributed to the disappearance of the C-type antiferromagnetic state ($T_N=150$ K). The 4.2 K curve clearly shows a second transition at lower magnetic field, also characterized by an irreversibility, which could be linked to the destruction of the small amount of the G-type antiferromagnetism ($T_N=70$ K). This observation was unexpected since only one metamagnetic transition is shown in the corresponding magnetization curve [Fig. 6(a)].

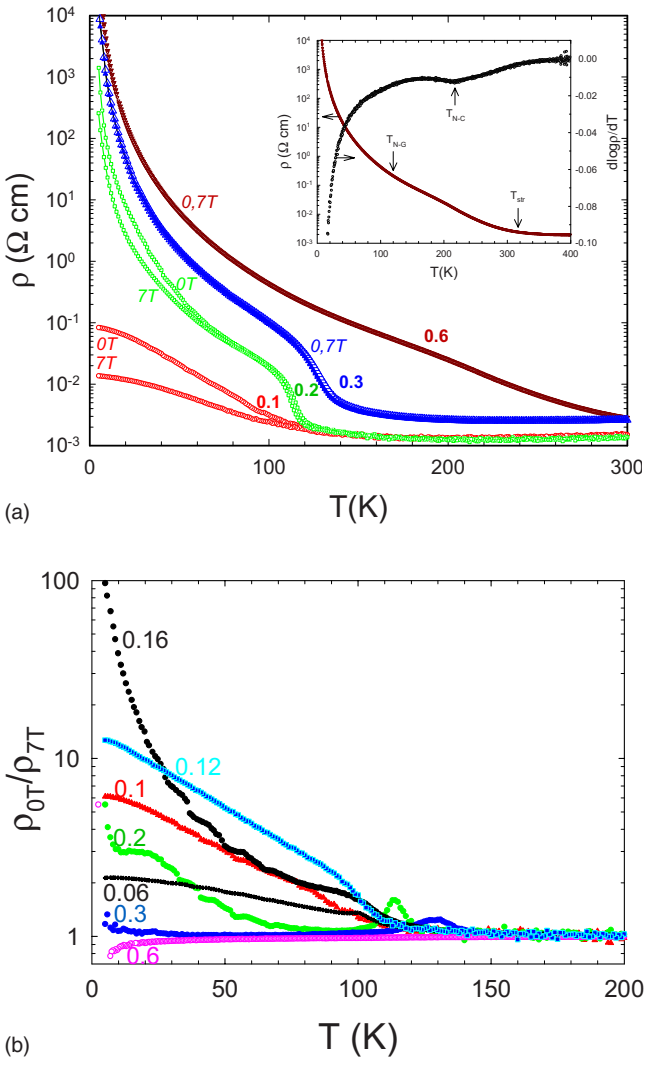

FIG. 9. (Color online) (a) T-dependent resistivity (ρ) curves of a selection of $Sm_{0.1}Ca_{0.9-x}Sr_xMnO_3$ samples (x values are given in the figure) in 0 or 7 T, decreasing temperature. Inset: $\rho(T)$ curve (right y axis) and corresponding $d\log\rho/dT(T)$ up to 400 K. (b) T-dependent MR values obtained by dividing data obtained upon cooling in 0 T ($\rho_{0\ \mathrm{T}}$) by data obtained in 7 T ($\rho_{7\ \mathrm{T}}$).

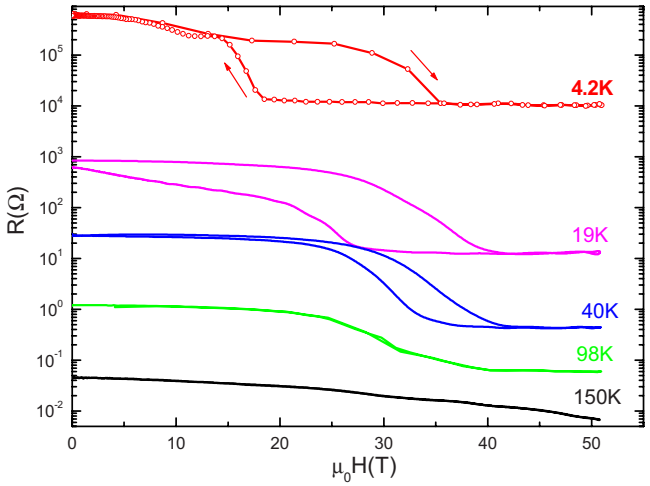

FIG. 10. (Color online) $Sm_{0.1}Ca_{0.6}Sr_{0.3}MnO_3$: High field resistance curves at several temperatures given in the figure.

Such $R(H)$ curves were not measurable for $Sm_{0.1}Ca_{0.3}Sr_{0.6}MnO_3$ due to its too insulating behavior. Its transport properties were thus completed by thermoelectric power measurements (Seebeck, S), which are compared to those of other Mn^{4+}-rich manganites (Fig. 11). At high temperature $[T_N(C) < T < 300$ K], i.e., in the paramagnetic state, the T-linear regime—observed in the metal-like state of $Sm_{0.1}Ca_{0.9}MnO_3$ (Fig. 11)—is not reached, probably in connection with the very broad structural transition observed in this temperature range for $Sm_{0.1}Ca_{0.3}Sr_{0.6}MnO_3$ (as described before). For the latter, the S minimum value (about $-66\ \mu V\ K^{-1}$) is observed for temperatures close to $T_N(C) \cong 240$ K, indicating that below that temperature the carrier localization related to the AF is starting. Decreasing T, S changes of sign reaching positive values, up to $150\ \mu V\ K^{-1}$. Such large positive thermoelectric power values associated with AF are always observed in the case of Sr-rich electron-doped manganites. It is illustrated by the very similar $S(T)$ curves of $Sm_{0.1}Ca_{0.3}Sr_{0.6}MnO_3$ and $Pr_{0.1}Sr_{0.9}MnO_3$ in Fig.

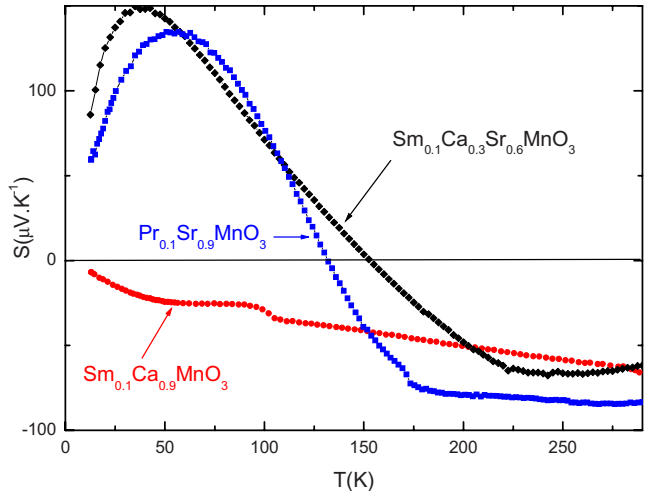

FIG. 11. (Color online) Thermopower curve $[S(T)]$ of $Sm_{0.1}Ca_{0.3}Sr_{0.6}MnO_3$, the $S(T)$ curves of $Sm_{0.1}Ca_{0.9}MnO_3$ and $Pr_{0.1}Sr_{0.9}MnO_3$ are given for comparison.

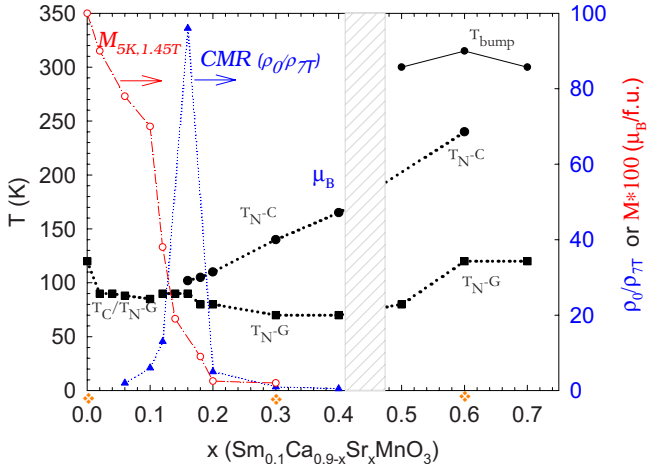

FIG. 12. (Color online) Phase diagram of $Sm_{0.1}Ca_{0.9-x}Sr_xMnO_3$, built from magnetic and transport measurements. The points studied by NPD ($x=0$, (Ref. 11) 0.3 and 0.6) are shown by (yellow) crosses. The CMR ratio (blue triangles) and value of magnetization at 5 K in 1.45 T are also reported (right y axis) to show the strong correlations between magnetism and transport properties.

11. As explained above, both samples are characterized by a similar low temperature state with a mixture of G- and C-AFs, but the higher mismatch in $Sm_{0.1}Ca_{0.3}Sr_{0.6}MnO_3$ leads to a destabilization of the G-AF, that does not appear in the $S(T)$ curves. Since similar $S \gg 0$ values are not observed in Ca-rich electron-doped manganites, this behavior is attributed to the A-site cation size effect on the electronic band structure, as reported in both electron-doped manganites, as in $Ca_{1-x}Sr_xMn_{0.96}Mo_{0.04}O_3$,[30] and hole-doped manganites.[31] In all cases, increasing the size of the A-site cations decrease, the structural distortion (as discussed in the first section for the present compounds), which affects the band structure. In the series under study, it seems difficult to go further in the interpretation due to the coexistence of two crystalline and magnetic phases for $Sm_{0.1}Ca_{0.3}Sr_{0.6}MnO_3$.

Discussion, $(\langle r_A \rangle, T)$ phase diagram, conclusion

The magnetic and structural phase diagram presented in Fig. 12 is built from the magnetic measurements described in this paper and the NPD results are added for $x=0$,[11] 0.3, and 0.6 (this study). There is a clear correlation between Figs. 1 and 12, showing the strong relationships between structures and properties in this $Mn^{+3.9}$ series.

With the Sr content increase, the average cationic radius of the A-site increases and a structural discontinuity—from *Pnma* to *I*4/*mcm*—is observed at the maximal mismatch value. Nevertheless, this change in the octahedral tilt system [from three tilt for *Pnma* to one tilt for *I*4/*mcm* (Ref. 32)] at room temperature is not linked to changes in the low temperature magnetic structure, as it was reported for the $Ln_{1/2}A_{1/2}MnO_3$ perovskites.[22] This behavior is similar to the one reported for the (Sr,Ca,Ba)MnO_3 series,[19] i.e., containing only Mn^{+4}, or for $Ca_{1-x}Sr_xMn_{0.96}Mo_{0.04}O_3$ (Ref. 30) (where the Mn valency is +3.92).

The ferromagnetic component, observed for $Sm_{0.1}Ca_{0.9}MnO_3$ in addition to the G-type AF, decreases pro-

gressively with x and vanishes for x close to 0.2. At this point, C-type antiferromagnetism appears that will coexist at low temperature with G-type AF. The T_N of the G component exhibits a small evolution, between 70 and 120 K, compared to the T_N of the C type which increases from 100 ($x=0.2$) to 240 K ($x=0.6$). Depending on x, the nature of the (crystallographic and magnetic) phase separation evolves; the distortion of the lattice increasing with x, the coexistence of different states should lead to particular microstructures at low temperatures.

The competition F/G-AF/C-AF gives thus various and puzzling properties, particularly for the small x values with the appearance of metastable diamagnetism for $x=0.06$, for instance.[33] The disappearance of F with x is also observable by the different pressure effects observed for $x=0.2$ and 0.3, compared to $x=0.1$.[34] Finally, such a study allowing the control between competing ground states is useful to maximize the colossal magnetoresistance (CMR) effect, it provides an alternative way to the optimization by changing the Mn valency (as in $Sm_{1-x}Ca_xMnO_3$).

[1] *Colossal Magnetoresistance, Charge Ordering and Related Properties of Manganese Oxides*, edited by C. N. R. Rao and B. Raveau (World Scientific, Singapore, 1998).

[2] *Colossal Magnetoresistive Oxides*, edited by Y. Tokura (Gordon and Breach Science, New York 1999).

[3] A. Maignan, C. Martin, F. Damay, and B. Raveau, Chem. Mater. **10**, 950 (1998).

[4] A. Maignan, C. Martin, F. Damay, B. Raveau, and J. Hejtmanek, Phys. Rev. B **58**, 2758 (1998).

[5] C. Martin, A. Maignan, F. Damay, M. Hervieu, and B. Raveau, J. Solid State Chem. **134**, 198 (1997).

[6] J. Hejtmanek, Z. Jirak, M. Marysko, C. Martin, A. Maignan, M. Hervieu, and B. Raveau, Phys. Rev. B **60**, 14057 (1999).

[7] J. Briático, B. Alascio, R. Allub, A. Butera, A. Caneiro, M. T. Causa, and M. Tovar, Phys. Rev. B **53**, 14020 (1996).

[8] J. J. Neumeier and J. L. Cohn, Phys. Rev. B **61**, 14319 (2000).

[9] E. O. Wollan and W. C. Koehler, Phys. Rev. **100**, 545 (1955).

[10] J. B. Goodenough, Phys. Rev. **100**, 564 (1955).

[11] C. Martin, A. Maignan, M. Hervieu, B. Raveau, Z. Jirak, M. M. Savosta, A. Kurbakov, V. Trounov, G. André, and F. Bourée, Phys. Rev. B **62**, 6442 (2000).

[12] C. D. Ling, E. Granado, J. J. Neumeier, J. W. Lynn, and D. N. Argyriou, Phys. Rev. B **68**, 134439 (2003).

[13] E. Granado, C. D. Ling, J. J. Neumeier, J. W. Lynn, and D. N. Argyriou, Phys. Rev. B **68**, 134440 (2003).

[14] Y. Moritomo, A. Machida, E. Nishibori, M. Takata, and M. Sakata, Phys. Rev. B **64**, 214409 (2001).

[15] E. Granado, N. O. Moreno, H. Martinho, A. Garcia, J. A. Sanjurjo, I. Torriani, C. Rettori, J. J. Neumeier, and S. B. Oseroff, Phys. Rev. Lett. **86**, 5385 (2001).

[16] http://journals.iucr.org/iucr-top/comm/cpd/Newsletters/ or http://www.ill.fr/pages/science/IGroups/diff/Soft/fp/.

[17] T. Negas and R. S. J. Roth, Solid State Chem. **1**, 409 (1970).

[18] M. Hervieu, C. Martin, A. Maignan, G. Van Tendeloo, Z. Jirak, J. Hejtmanek, A. Barnabé, D. Thopart, and B. Raveau, Chem. Mater. **12**, 1456 (2000).

[19] O. Chmaissem, B. Dabrowski, S. Kolesnik, J. Mais, D. E. Brown, R. Kruk, P. Prior, B. Pyles, and J. D. Jorgensen, Phys. Rev. B **64**, 134412 (2001).

[20] R. D. Shannon, Acta Crystallogr., Sect. A: Cryst. Phys., Diffr., Theor. Gen. Crystallogr. **32**, 751 (1976).

[21] Z. Jirak, S. Krupicka, Z. Simsa, M. Dlouha, and S. Vratislav, J. Magn. Magn. Mater. **53**, 153 (1985).

[22] P. M. Woodward, T. Vogt, D. E. Cox, A. Arulraj, C. N. R. Rao, P. Karen, and A. K. Cheetham, Chem. Mater. **10**, 3652 (1998).

[23] L. M. Rodriguez-Martinez and J. P. Attfield, Phys. Rev. B **54**, R15622 (1996).

[24] L. M. Rodriguez-Martinez and J. P. Attfield, Phys. Rev. B **58**, 2426 (1998).

[25] F. Damay, C. Martin, A. Maignan, M. Hervieu, B. Raveau, Z. Jirak, G. André, and F. Bourée, Chem. Mater. **11**, 536 (1999).

[26] C. Martin, A. Maignan, M. Hervieu, B. Raveau, Z. Jirak, A. Kurbakov, C. André, and F. Bourée, J. Magn. Magn. Mater. **205**, 184 (1999).

[27] P. W. Stephens, J. Appl. Crystallogr. **32**, 281 (1999).

[28] M. Respaud, J. M. Broto, H. Rakoto, J. Vanacken, P. Wagner, C. Martin, A. Maignanand, and B. Raveau, Phys. Rev. B **63**, 144426 (2001).

[29] W. Bao, J. D. Axe, C. H. Chen and S.-W. Cheong, Phys. Rev. Lett. **78**, 543 (1997).

[30] M. Miclau, S. Hébert, R. Retoux, and C. Martin, J. Solid State Chem. **178**, 1104 (2005).

[31] J. Hejtmanek, Z. Jirak, D. Sedmidubsky, A. Maignan, Ch. Simon, V. Caignaert, C. Martin, and B. Raveau, Phys. Rev. B **54**, 11947 (1996).

[32] P. M. Woodward, Acta Crystallogr., Sect. B: Struct. Crystallogr. Cryst. Chem. **53**, 32 (1997).

[33] V. Markovich, I. Fita, R. Puzniak, C. Martin, K. Kikoin, A. Wisniewski, S. Hébert, A. Maignan, and G. Gorodetsky, Phys. Rev. B **74**, 174408 (2006).

[34] V. Markovich, I. Fita, R. Puzniak, C. Martin, A. Wisniewski, S. Hébert, A. Maignan, and G. Gorodetsky, J. Phys.: Condens. Matter **18**, 9201 (2006).